Research article

Optimizing inferior vena cava filter design: A computational fluid dynamics study on strut configuration for enhanced hemodynamic performance and thrombosis reduction

Byeong-Jun Kim [a], Chiseung Lee [b,c,*]

[a] *Department of Biomedical Engineering, Graduate School, Pusan National University, Busan 49241, Republic of Korea*
[b] *Department of Biomedical Engineering, School of Medicine, Pusan National University, Busan 49241, Republic of Korea*
[c] *Biomedical Research Institute, Pusan National University Hospital, Busan 49241, Republic of Korea*

ARTICLE INFO

ABSTRACT

Background and objective: Inferior vena cava filters have been shown to be effective in preventing deep vein thrombosis and its secondary complication, pulmonary embolism, thereby reducing the high mortality rate. Although inferior vena cava filters have evolved, specific complications like inferior vena cava thrombosis-induced deep vein thrombosis worsening and recurrent pulmonary embolism continue to pose challenges. This study analyzes the effects of geometric parameter variations of inferior vena cava filters, which have a significant impact on the thrombus formation inside the filter, the capture, dissolution, and hemodynamic flow of thrombus, as well as the shear stress on the filter and vascular wall.

Methods: This study used computational fluid dynamic simulations with the carreau model to investigate the impact of varying inferior vena cava filter design parameters (number of struts, strut arm length, and tilt angle) on hemodynamics.

Results: Recirculation and stagnation areas due to flow velocity and pressure, along with wall shear stress values, were identified as key factors. It is important to find a balance between wall shear stress high enough to aid thrombolysis and low enough to prevent platelet activation. The results of this paper show that the risk of platelet activation and thrombus filtration may be lowest when the wall shear stress of the filter ranges from 0 to 4 [Pa], minimizing stress concentration within the filter.

Conclusion: 16 arm struts with a length of 20 mm and a tilt angle of $0°$ provide the best balance between thrombus capture and minimization of hemodynamic disturbance. This configuration minimizes the size of the stagnation and recirculation zones while maintaining sufficient wall shear stress for thrombus dissolution.

1. Introduction

The inferior vena cava (IVC), a large vein in the thoracoabdominal region, is implanted with a medical device called an IVC filter to capture and prevent emboli and thrombi from traveling to the lungs deep vein thrombosis (DVT) and pulmonary embolism (PE) are collectively known as venous thromboembolism (VTE), which is the third leading cause of cardiovascular-related death, following

---

myocardial infarction and stroke [1]. DVT is a blood clot that forms in a deep vein, usually in the leg. A blood clot that breaks off from a DVT can travel to the lungs and block a pulmonary artery, causing a PE [2].

The most common treatment for PE and DVT is anticoagulation therapy, which uses medications to thin the blood and reduce the risk of clotting (e.g., warfarin and heparin). Before resorting to an IVC filter, the 2019 ESC guidelines emphasize that VTE patients should first be offered anticoagulation therapy. Only if this proves impossible or ineffective, due to contraindications or recurring PE, is filter placement recommended [3]. While some small trials suggest short-term benefits of IVC filters in preventing PE after trauma surgery, conclusive evidence for long-term efficacy remains elusive due to the absence of large-scale randomized controlled trials [4, 5]. This shows that IVC filter use can be associated with many complications, including thrombosis.

Modern inferior vena cava filters (IVCFs) come in a variety of designs and can have different hemodynamic effects. Design characteristics such as thrombosis prevention, complication minimization, and hemodynamics are interrelated and have been extensively studied using design optimization parameters [6,7].

First, in terms of thrombosis prevention, the larger surface area filter of the IVCF captures more emboli, potentially reducing the risk of PE. However, filters may increase blood flow obstruction and therefore require patient-specific application. To capture clots effectively, increasing the density of the filter can better capture clots, while open designs allow for better flow but may miss smaller clots [8].

Second, in terms of minimizing complications, retrievable filters can be removed if the risk of PE is low, reducing the risk of long-term complications such as vena cava thrombosis. However, there are some risks associated with filter recovery. And according to the thick support structure of the strut filter, it can not only increase the cavalry occlusion, but also provide better structural stability. Conversely, thin braces may have a lower hemodynamic profile but are more likely to result in fractures. Additionally, a well-fixed filter is less likely to tilt or move within the vena cava, reducing the risk of complications such as vena cava perforation or damage to surrounding vascular structures [9].

Third, from a hemodynamic perspective, the number, length, and diameter of filter struts impact blood flow disruption. Tilted filters can cause uneven flow distribution, potentially increasing thrombosis risk by promoting clot growth at specific filter points. Additionally, the pressure drop across the filter (upstream vs. downstream flow) can worsen DVT. Finally, the magnitude of wall shear stress (WSS) can influence clot growth and dissolution [10].

To address this, the performance of the filter should be clearly studied and improved using computational mechanics such as finite element method (FEM) and computational fluid dynamic (CFD). Despite being so widely used, there are no published studies on the design of IVC filters that are optimally designed in terms of the number, length, and angle of filter struts based on hemodynamic considerations.

Most studies on IVC filters have focused on varying strut shape, specific region geometry, or blood rheology (Newtonian vs. non-Newtonian) while introducing actual thrombi. This study investigates the hemodynamic changes induced by increasing strut number and length in a single filter to mitigate thrombotic risk. Assuming a wider surface area and higher density, we numerically evaluate thrombus stagnation zones, velocity, and pressure drop at specific filter points under constant blood velocity and pressure. We also analyze the impact on thrombus capture performance and flow dynamics and assess the influence of tilted filter orientation on blood flow in the vessel. Based on the assumption that thrombus viscosity is inversely correlated with shear rate, we use WSS and molecular viscosity to analyze thrombus formation and specific locations on the filter from a hemodynamic perspective.

The blood clot capture performance of an IVC filter is critically dependent on the way the blood clot flows through the IVC and the underlying hemodynamics. Therefore, the thrombogenicity is correlated with hemodynamic conditions such as high/low WSS and stagnant/recirculating flow regions [1,11]. As a result, from a hemodynamic perspective, the optimally designed filter is a filter that traps blood clots in a configuration that minimizes the effects of these abnormal flow conditions, thereby minimizing the risk of IVC occlusion. In addition, theoretical modeling and CFD-based design optimization development methods for filters are convenient methods to minimize hemodynamic disruption, and are also less expensive than in vivo and in vitro experiments [12–15]. According to the existing literature, very high shear stress can activate platelets and lead to thrombosis, which can completely block blood flow. In the arterial circulation, increased blood flow leads to higher shear stress, which contributes to the dilution of certain pro-coagulant molecules, preventing the formation of insoluble fibrin. In areas of low wall shear stress, stagnation, and recirculating flow, it supports the accumulation of thrombin and fibrin, potentially leading to thrombosis [16,17]. The efficacy and stability of IVCFs after placement continue to be a problem in modern medicine, and local hemodynamics near the filter play an important role in determining filter efficacy [18,19].

This paper presents a CFD simulation of IVC filter hemodynamics, implemented using the popular Ansys Fluent software. The impact of varying filter strut parameters (number, length, and angle) on blood flow dynamics, including velocity, WSS, pressure, and viscosity, was explored through simulations. The results are then used to investigate the hemodynamics of blood clot formation and the viscous block effect in the filter. Therefore, CFD can be used to evaluate the potential side effects of IVC filters, such as thrombus formation or vascular damage.

2. Materials and methods

2.1. Inferior vena cava filter

A generic IVCF (US FDA, Confluent Medical: Brent Craven, Jason Weaver, Kenneth Aycock) was created as a 3D model (Dassault System SolidWorks Corporation, Waltham, MA, USA) in the form of a Mock-IVC by a team from the US FDA and Confluent Medical for filter research [20]. As shown in Fig. 1, IVC filters are composed of two main parts: a head, through which blood flows out of the filter,

and leg struts, which contact the wall of the vein. The arms, which are responsible for embolic filtration, are included in the leg struts. The first parameter, the arm strut count of the filter used in the study was 4 cases: 8, 12, 16, and 20 arm struts. The second parameter, the angle between the vein wall and the filter, was 0, 8, or 19°, and the third parameter, the length of the arm, was 10, 20, or 30 mm. The total length of the standard 16-arm strut filter is 35 mm, with a head of 5 mm, arms of 20 mm, wall contact struts of 10 mm, head outer diameter of 2.03 mm, inner diameter of 1.33 mm, and thickness of 0.35 mm.

The scope of the present investigation will be restricted to a simplified model that excludes the contributions of complex physiological factors such as side branch formation, IVC deformation, and respiration-induced IVC collapse. Therefore, we need to make some basic assumptions about the CFD simulation [21,22].

In contrast to actual IVC filters, which employ fixed hooks for secure attachment to the vessel wall, 3D models utilized in CFD simulations often disregard this structural component.

Second, for consistency with past research, the IVC took the form of a rigid, 20 mm-diameter cylinder in our 3D model.

Third, to achieve a realistic flow profile and avert unrealistic boundary influences within the simulation, we incorporated lengthy flow extensions, each measuring roughly 20 times the diameter (D), at both the inlet and outlet sections [23].

The CFD simulations, informed by realistic assumptions that mirror actual IVCF procedures, yield reliable and valuable insights into IVCF flow dynamics within the IVC.

2.2. Governing equations

Blood is a non-Newtonian fluid that exhibits shear thinning behavior, in which the viscosity decreases with increasing shear rate. This is due to the rearrangement of the microscale geometry of the blood under the influence of shear stress. For large arteries, a simpler "Newtonian" model is often used to describe blood flow instead of a more complex "non-Newtonian" model [24]. Limitations of the Newtonian model become apparent when simulating IVC hemodynamics, especially for WSS, necessitating the use of more sophisticated models to capture the nuanced flow behavior [25]. In this study, the Carreau model was found to be the best approach for capturing the asymptotic behavior of shear-thinning fluids at both low and high shear rates. This distinguishes the Carreau model from other models (Newtonian, power-law, cross, etc.) that are widely used in blood flow modeling [26–29]. Therefore, Blood flow within an IVC filter is modeled as a viscous and incompressible fluid governed by the Navier-Stokes equation (1), ensuring conservation of mass and momentum.

The gradient operator (∇) applied to the blood flow velocity vector (V) represents the rate of change of flow speed and direction across space. This, along with blood density (ρ) and static pressure (p), contribute to the viscous stress tensor (τ) through Equation (2) [30],:
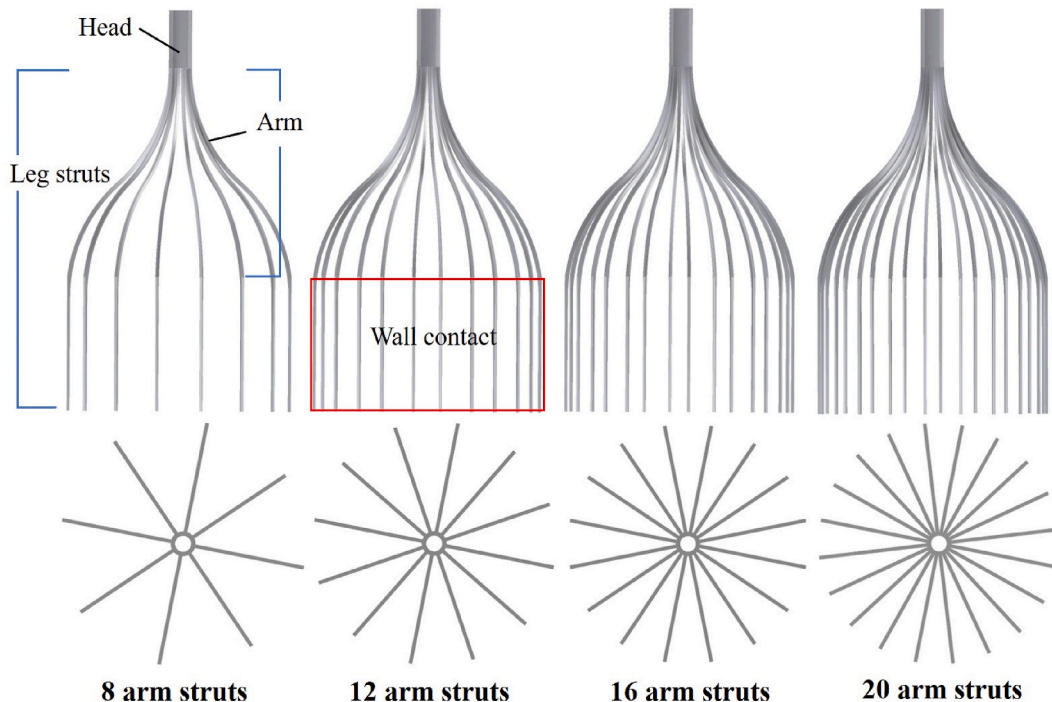

Fig. 1. Generic IVCFs, which are composed of a head, leg struts, and arms, were modeled as geometric 3D models with 8, 12, 16, and 20 arm struts.

$$\begin{cases} \nabla \cdot \mathbf{V} = 0 \\ \rho \mathbf{V} \cdot \nabla \mathbf{V} = -\nabla p + \nabla \cdot \tau \end{cases} \tag{1}$$

$$\tau = \mu \left[\nabla \mathbf{V} + (\nabla \mathbf{V})^{\mathbf{T}} \right] \tag{2}$$

Where μ represents the dynamic viscosity of blood, and the superscript "T" represents the transpose of a matrix. Blood is a non-Newtonian fluid, so its viscosity changes depending on the flow shear rate. To use the Carreau model, the following equation (3) is used to calculate the dynamic viscosity μ of blood. Blood density (ρ): 1060 kg/m3, dynamic viscosity (μ): 0.00345 Pa s, local shear rate (γ), power law index (n): 0.3568, time constant (λ): 3.313 s, infinite shear viscosity (μ_∞): 0.00345 Pa s, and zero shear viscosity (μ_0): 0.056 Pa s [31].

A go-to choice for blood rheology simulations, the Carreau model, backed by extensive validation studies, accurately captures the non-Newtonian behavior of this complex fluid. It has been shown to be adequately accurate in describing the shear-thinning behavior of blood.

$$\mu = \mu_\infty + (\mu_0 - \mu_\infty) \left[1 + (\lambda\gamma)^2 \right]^{\frac{n-1}{2}} \tag{3}$$

Fig. 2 shows a 16-arm struts IVCF that is implanted in the IVC. Blood flows from the inlet to the outlet. The boundary conditions for the blood flow are no-slip walls at the entire surface of the filter and the vessel wall.

The IVC was modeled as a straight, rigid tube with an internal diameter of 20 mm, based on the average venous diameter described by Kaufman et al. [32]. The length of the tube is 170 mm, which provides an adequate distance for the inlet velocity profile to fully develop before reaching the filter.

The velocity inlet condition in Fluent is set to an average velocity of 0.06 m/s, which corresponds to a volumetric flow rate of approximately 1.13 L/min [33].

To mimic realistic hemodynamics, the inlet velocity in our simulation reflects human IVC measurements. At the outlet, assuming fully developed flow, we relied on extrapolated interior data with zero diffusion flux for all flow variables.

The mathematical heart of our IVC blood flow simulation lies in equations (1)–(3), a trio that captures fluid dynamics. Ansys Fluent expertly solves these equations, factoring in boundary conditions that mirror real-world constraints. The results show that the spatial averaged viscosity (μ_a) is 0.0078 Pa s and the Reynolds number is 163. This indicates laminar flow in all cases.

2.3. Computational mesh

The 3D geometry of IVC and IVCF needs to be divided into a large number of small volumes (cells) or nodes. This task has typically been implemented in commercial pre-processing tools using tetrahedral and hexahedral shapes, depending on the target shape.

Unfortunately, these meshing tasks can be time-consuming and it may be impossible to generate good-quality cells for complex shapes. On the other hand, the polyhedral cells applied in this paper were used to overcome the disadvantages of both mesh types by combining the advantages of tetrahedral cells (fast calculation speed but low accuracy) and hexahedral cells (slow calculation speed but high accuracy).

The main advantages of polyhedral meshes are, firstly, each that individual cell has many neighbors, which allows for better approximation of gradients. Secondly, Polyhedral meshes are less sensitive to stretching than tetrahedral meshes, which improves mesh quality and leads to improved numerical stability of the model. Thirdly, Polyhedral meshes can achieve a given accuracy with fewer cells than tetrahedral meshes [34,35]. Thus, due to its complex geometric structure that accurately reflects the thin supports, arms, and head of an IVC filter, the polyhedral mesh is better suited to simulating blood flow around these intricate curves and bends compared to simpler tetrahedral meshes. This enhanced geometric accuracy leads to a more realistic simulation of blood-filter interaction, enabling more accurate predictions of filter performance. Additionally, the polyhedral mesh's accuracy improves filter design by allowing for a more precise simulation of results (velocity, pressure, WSS, etc.) within the filter [36,37].

Fig. 3 shows the mesh of the IVC and IVCF models for CFD simulations. As described above, the meshes were interpreted by
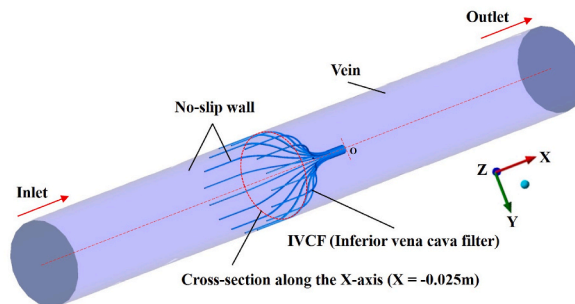

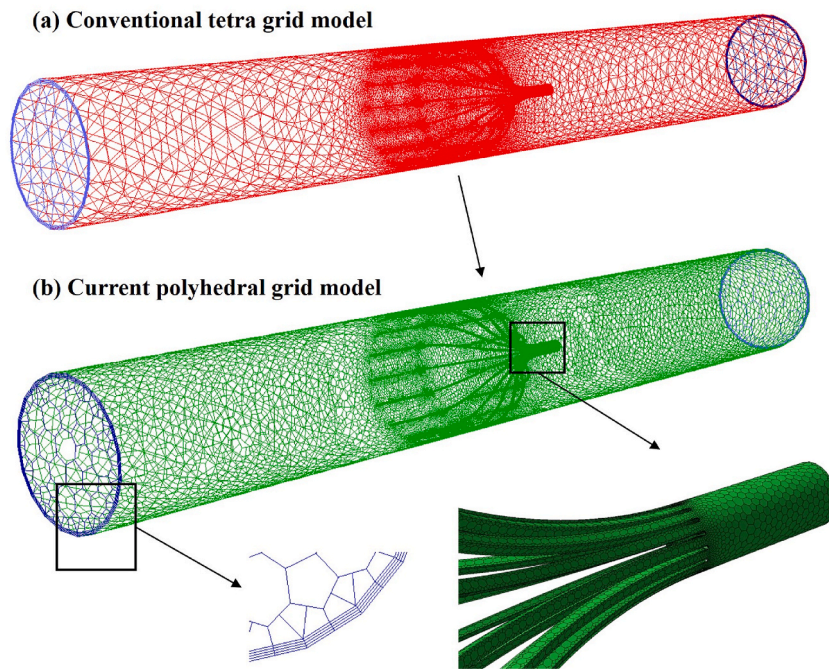**Fig. 2.** IVCF-implanted IVC and blood flow boundary conditions.

Fig. 3. IVC and IVCF grids for CFD simulations.

changing from Fig. 3(a) tetra grids to Fig. 3(b) polyhedral grids for accurate results, mesh quality, and fast calculation. Blood flow is mainly significantly changed in the vicinity of the IVCF filter and in the vascular wall where it stagnates locally. Therefore, four layers were created on the wall of the IVC, and the finest mesh was created around the filter.

CFD software FLUENT (ANSYS, Inc., Canonsburg, PA, United States) uses a coupled pressure-velocity coupling method, which uses a pseudo transient algorithm to have an implicit under-relaxation form for steady-state fluids, which helps with stability and fast convergence.

The simulations were performed on a workstation (AMD Ryzen Threadripper 3990X 64-Core Processor, 2.90 GHz) with 64 cores and 128 threads. The convergence residue was set to 10^{-6}, and each case took about 1 day to complete the analysis.

2.4. Mesh independence study

To select the appropriate mesh structure and size, which are essential for the accuracy and convergence of the numerical solution, CFD model independence evaluation was performed to identify the excellent state by increasing the number of meshes using Richardson extrapolation method [35,38].

The minimum refinement ratio (r) was recommended to be 1.3 by Celik et al. The mesh residual convergence criterion for the Generic IVC model arm struts (1–4 cases) was 1E-06. The mesh type gradually refined into 6 types per case, and in Table 1, it was shown as three types: coarse, medium, and fine.

Table 1
Evaluation of CFD model grid independence with respect to the number of IVCF arm struts.

Generic IVC		Mesh type	Number of Cell	Max. velocity [m/s]	Area-weighted average WSS (IVC wall) [Pa]	Area-weighted average WSS (IVCF) [Pa]	Refinement ratio ($r \geq 1.3$)
case1	8 arm struts	Coarse	6.93E + 05	0.0963	0.2330	0.8285	$G_{medium}/G_{coarse} =$
		Medium	1.06E + 06	0.1000	0.2204	0.8693	1.53
		Fine	2.62E + 06	0.1005	0.2180	0.8738	$G_{fine}/G_{medium} = 2.48$
case2	12 arm struts	Coarse	8.79E + 05	0.0968	0.2387	0.8729	$G_{medium}/G_{coarse} =$
		Medium	1.31E + 06	0.1009	0.2260	0.9145	1.49
		Fine	2.91E + 06	0.1010	0.2227	0.9211	$G_{fine}/G_{medium} = 2.22$
case3	16 arm struts	Coarse	1.01E + 06	0.0976	0.2436	0.8988	$G_{medium}/G_{coarse} =$
		Medium	1.45E + 06	0.1012	0.2319	0.9398	1.43
		Fine	3.05E + 06	0.1017	0.2271	0.9467	$G_{fine}/G_{medium} = 2.12$
case4	20 arm struts	Coarse	1.15E + 06	0.0991	0.2499	0.9010	$G_{medium}/G_{coarse} =$
		Medium	1.53E + 06	0.1027	0.2371	0.9431	1.33
		Fine	3.04E + 06	0.1032	0.2316	0.9527	$G_{fine}/G_{medium} = 1.99$

The 1–4 cases all satisfied the Richardson extrapolation refinement ratio of r ≥ 1.3. Fig. 4 shows a cross-section of the IVC at the X-axis position of −0.025 m in Fig. 2. The maximum velocity size was quantitatively calculated according to the increase in nodes. Figs. 5 and 6 show the area-averaged WSS of IVC and IVCF, respectively. That is, the shear stress acting on the vascular wall and the filter wall. As the number of grid nodes increases, the maximum velocity of 8, 12, 16, and 20 arm struts increases sharply up to the medium mesh number, and then the speed change becomes very small until the fine mesh number is reached. And as the number of struts increases, the speed size also increases proportionally. The graphs of area average IVC WSS and area average IVCF WSS are also similar in terms of the relationship between the number of meshes and the change in WSS size. However, as the number of struts increases, the size of the area average IVC WSS decreases and the size of the area average IVCF WSS increases. The results convincingly show that both the maximum velocity and the filter's area-averaged WSS steadily approach their true, accurate values as the mesh resolution is refined, ultimately converging towards the solution that would be obtained with an infinitely fine mesh. In particular, the WSS value is the parameter that has the greatest influence on the filtration of thrombi. Fig. 5 shows that the change in the WSS values available on the IVC wall for cases 1–4 is very small, ranging from 0.22 to 0.23 (Pa), as the number of nodes increases. However, as the number of nodes increases, the WSS values converge to a constant performance value. Additionally, the WSS values in the IVCF, which is of greatest interest to us, show the best performance in cases 3 (arm strut 16) and 4 (arm strut 16), as shown in Fig. 6. Therefore, in this study, 8, 12, 16, and 20 arm struts were judged to be superior in terms of performance and economic efficiency in the hemodynamic results with increasing number of nodes. Therefore, for all cases, the total number of grid nodes for the IVC and IVCF models was set to approximately 3 million, and arm strut 16 was selected as the representative model.

3. Results

3.1. Blood velocity

The blood velocity results around the IVCF are divided into 10 cases, which are mainly classified into three categories (strut number, arm length, and tilted angle). Using a plane intersecting the IVC diameter, Figs. 7 and 9 present the distribution of blood velocity at the filter's cross-section (axial profile) and along its entire length, focusing on the point with zero radius (r = 0).

Fig. 7 illustrates the variation in blood flow velocity distribution with increasing arm struts (from 8 to 20). To better visualize and compare the downstream flow patterns, Fig. 8 depicts the streamlines of the velocity distribution. The highest velocities occur within the filter (high-velocity region), while the slowest flow is observed near the filter head. In particular, the strongest flow of speed is observed on the inner surface where the diameter of the filter internal strut decreases, and conversely, a stagnation and recirculation region occurs in the head region due to the influence of slow speed. As shown in Fig. 7(a), the size of the blue region with the lowest velocity inside the red circle, which is the stagnation and recirculation region around the head, gradually increases as the number of arm struts increases. The size of the blue region (upstream of the filter head) is larger in the region connected to the arm struts than in the head region that is not connected to the arm struts.

In addition, as the number of arm struts increases, the blue rectangular region in Fig. 7(a) showed an increase in velocity up to 8, 12, and 16-arm struts, followed by a decrease in 20-arm struts. Fig. 7(b) shows the blood flow velocity distribution in cross-section for the 16-arm struts. The overall velocity distribution results of the four filters were similar.

As shown in Fig. 7(b), the flow on the filter surface travels downstream from the inlet (sections 1-7). Due to blood viscosity, emboli (debris or clots) are concentrated towards the center of the filter between the struts, where the velocity increases. The velocity of these emboli collected inside the struts decreases as they move closer to the vessel wall. The blood encounters the struts upon entering the filter, creating a viscous blocking effect. This effect helps concentrate the emboli towards the center (sections 1-3) and subsequently reduces the internal velocity (sections 3-7). At section 4, the flow velocity exhibits a rapid reversal inside and outside the arm strut
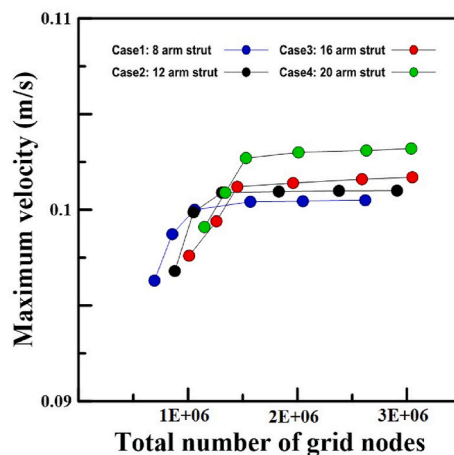

Fig. 4. Maximum velocity at the cross-section at z = −0.025 m, by node count.
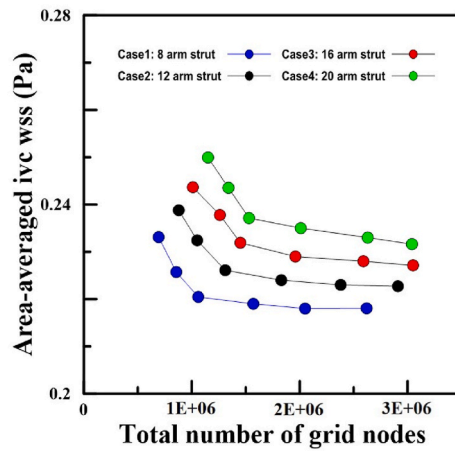
Fig. 5. Area-averaged wall shear stress on the IVC wall, as a function of node count.
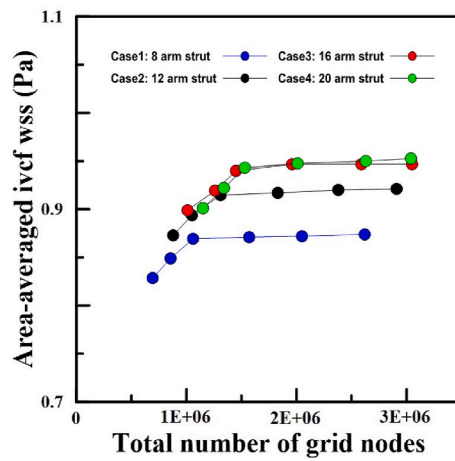

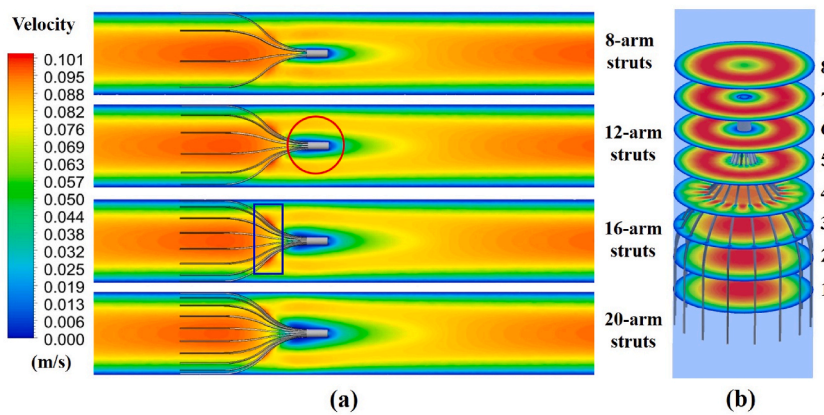**Fig. 6.** Area-averaged wall shear stress on the IVCF wall, as a function of node count.

Fig. 7. (a) Distribution of blood flow velocity in the axial section according to the number of struts and **(b)** in the cross-sections according to the 16-arm struts.
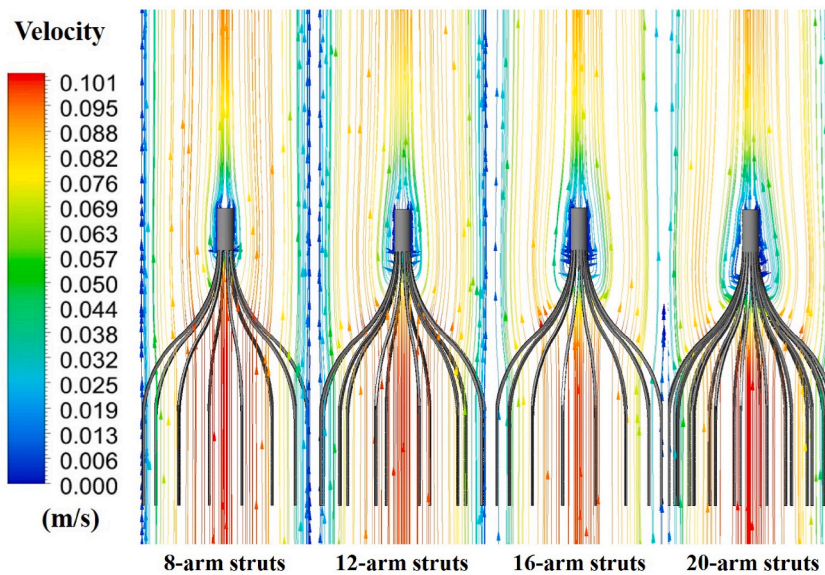
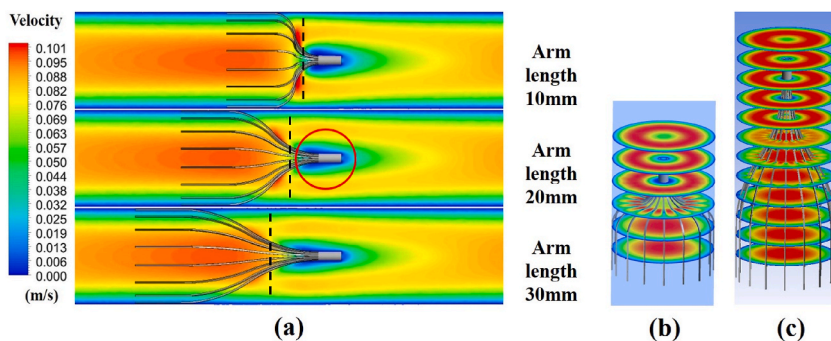**Fig. 8.** Streamlines of blood flow velocity in the axial section according to the number of struts.

Fig. 9. (a) Distribution of blood flow velocity in the axial section according to the arm length, **(b)** in the cross-sections according to the 10 mm arm length and **(c)** 30 mm arm length.

(blue box in Fig. 7(a)). The internal velocity at section 4 is low, while the external velocity gradually increases, leading to the development of a recirculation zone near the external surface of the head. As illustrated in Fig. 7(a), increasing the number of arm struts proportionally increases the volume of the area where emboli can stagnate (stasis zone) and the recirculation area. However, the velocity of the blue rectangular region in Fig. 7(a) does not increase proportionally.

Fig. 9 shows the blood flow velocity distribution in cross-section and in plane according to arm length. Fig. 9(a) is a model with an arm length of 20 mm, which is the same model as the 16-arm struts in Fig. 7(a)–and is the baseline model for this paper. As the length of the arm increases from 10 mm to 30 mm, the volume of the stagnation zone and recirculation area decreases. The shape of the red circle area in Fig. 9 also changes from a streamlined shape at 10 mm to a sharper streamlined shape, with different overall shape and volume. The black dotted line in Fig. 9(a) is the line where the blood flow that enters the filter interior first meets the struts and the stagnant and recirculating areas of the fully developed head region are clearly divided due to the viscous block effect [39,40]. This dotted line develops downwards to the inlet side (upstream of the filter) as the arm length increases. For the same reason, the shape of the blood flow velocity at the plane of the filter with arm lengths of 10 mm and 30 mm in Fig. 9(b) and (c) also occurs first on the upstream of the filter as it goes from 10 mm to 30 mm (higher velocity between filter struts).

As shown in Fig. 9(a), increasing the arm length from 10 mm to 30 mm enlarges the filtration area, which enhances the filter's ability to capture emboli (debris or clots). However, as indicated by the red circle, thrombus formation decreases around the head with increasing arm length, and thrombus formation occurs more in the upstream region than in the downstream region. Therefore, the selection of an appropriate filter depends on the individual patient's hemodynamic characteristics to balance thrombus formation and capture.

IVCF aims to minimize blood flow interruption, effectively prevent fatal PE, and prevent thrombosis and complications. The ideal placement of an IVCF is generally considered to be when the upper surface of the filter head is perpendicular to the vessel wall ($\alpha = 0°$),
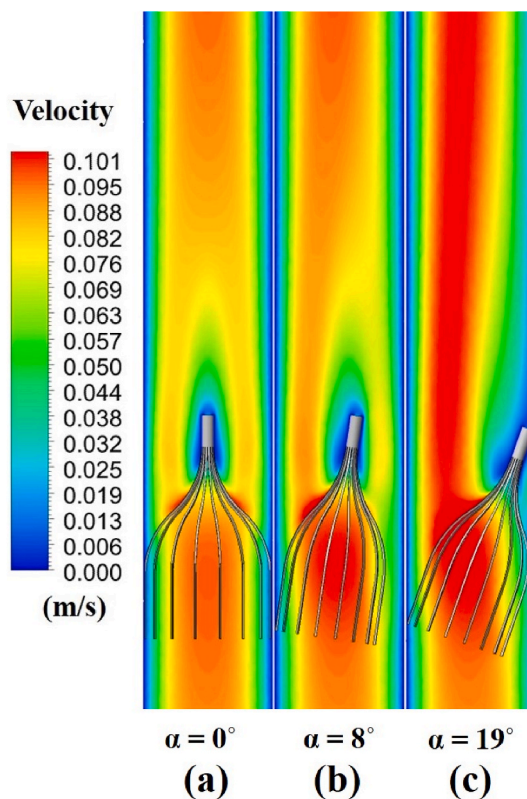
Fig. 10. Distribution of blood flow velocity in the axial section according to the tilted IVCF angle.

as shown in Fig. 10(a). This placement allows the filter to be located in the center of the vessel, trapping thrombi away from the vessel wall in the central vein. However, scoliosis, venous angulation, or external factors can cause it to tilt.

The results of Fig. 10 show that the flow of blood entering the filter is fully developed and a flow with a velocity of 0 is observed at the vessel wall and around the filter, especially at the filter head. As the filter tilts by $\alpha = 8°$, as shown in Fig. 10(b), the symmetric flow around the filter is broken and the stagnant zone around the filter head increases. Also, the flow inside the filter increases in velocity towards the opposite arm struts of the tilt, resulting in stronger velocity and pressure on one side of the struts than when it is in the state of Fig. 10(a). Fig. 10(c) shows the filter at an angle of $\alpha = 19°$, which is the maximum tilt. The flow velocity towards the opposite side of
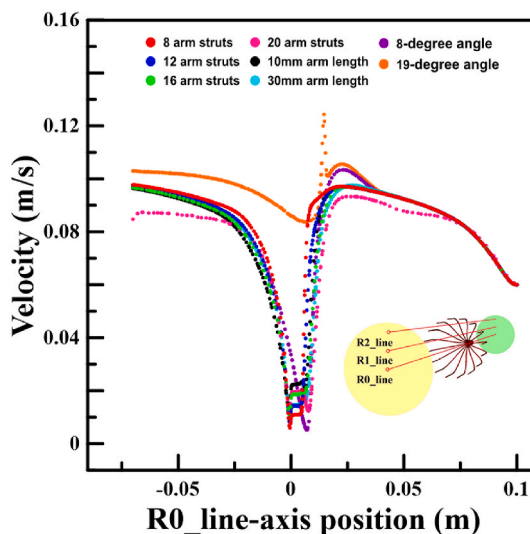

Fig. 11. Blood flow velocity on the central line (R0_line) of the 8 cases.

the filter is even greater than that in Fig. 10(b). In particular, a large stagnant flow is observed in the area of the filter head that is tilted towards the vessel wall. Between the head that is touching the vessel and the arm struts, the flow velocity is not zero, but it is significantly slower than in the rest of the filter. The low-speed flow in these regions can cause blood particles to stay in the filter for a longer period of time, which can lead to platelet aggregation.

Figs. 11–13 investigate the role of key IVCF parameters, namely arm struts, arm length, and tilt angle, in influencing hemodynamics. R0, R1, and R2 represent measurement points located at the center line and near the vessel wall, respectively, revealing variations in blood flow velocity. In all graphs, blood flow entering the IVC flows from position 0.1 m (inlet) on the graph's horizontal axis to position −0.075 m (outlet).

Fig. 11 shows that for all parameter variations except 8° and 19° tilts, blood entering the IVC at 0.06 m/s accelerates up to around 0.095–0.099 m/s before reaching the inner arm struts within the filter. At the point where it first meets the inner arm struts, the blood with high speed is broken down by viscosity and the speed decreases to about 0.01–0.022 m/s at the point where the filter head starts. After that, the speed remains at a constant speed of about 0.01–0.022 m/s for a length of the head until 0.005 m, and then drops to the lowest speed again at the end of the head. The reduced blood flow velocity passes through a streamline-shaped recirculation and stagnation area, such as the red circle in Fig. 9(a), and then rises sharply and escapes.

The change in blood flow velocity at the R0_line according to the three parameters is as follows.

First, the increase in the number of arm struts had the effect of increasing the speed from the point where it first meets the struts inside the IVCF to the end of the head. Therefore, the speed increased at a constant rate of about 0.005 m/s until 16 arm struts, and there was little difference between 16 and 20 arm struts.

Second, in contrast, for 10, 20, and 30 mm arm length, the speed decreased at a constant rate as the arm length increased.

Third, as the tilted filter angle increased from 0 to 8–19°, the speed R0 line changed the position of the minimum and maximum speeds, but was similar to 0° due to the tilted shape and imbalance of the speed flow.

As shown in Fig. 12, the change in blood flow velocity at the R1_line according to the three parameters is as follows. Blood entering the IVC inlet at 0.06 m/s accelerates up to around 0.089–0.119 m/s before reaching the inner arm struts within the filter, excluding 8° and 19° tilts. At the point where it first meets the inner arm struts, the blood with high speed is broken down by viscosity and the speed decreases to around 0.057–0.088 m/s.

The change in blood flow velocity at the R1_line according to the three parameters is as follows.

First, the increase in the number of arm struts increased the speed from the point where it first meets the struts inside the IVCF to 8, 12, and 16 arm struts, but the speed of 20 arm struts decreased.

Second, for 10, 20, and 30 mm arm length, the point where it first meets the struts is advanced as the arm length increases, and the maximum speed decreases.

Third, as the tilted filter angle increases from 0 to 8–19°, the speed R1 line is observed that the maximum speed is observed at the arm struts opposite the wall where the filter is close, and the range of high-level speed flowing to the struts also increases.

As shown in Fig. 13, the change in blood flow velocity at the R2_line according to the three parameters is as follows. Blood entering the IVC inlet at 0.06 m/s accelerates to 0.07 m/s at the entrance of the filter, then decreases sharply to about 0.048–0.051 m/s until it first meets the inner arm struts. After that, the speed increases sharply to about 0.059–0.075 m/s until the filter head, and then drops sharply again to the exit.

The change in blood flow velocity at the R2_line according to the three parameters is as follows.

First, the increase in the number of arm struts resulted in a similar decrease in the speed of about 0.048 m/s until the struts inside the IVCF, except for 20 arm struts. After that, the flow to the top of the head increased from 8 to 12 to 16, but at 20 arm struts, it
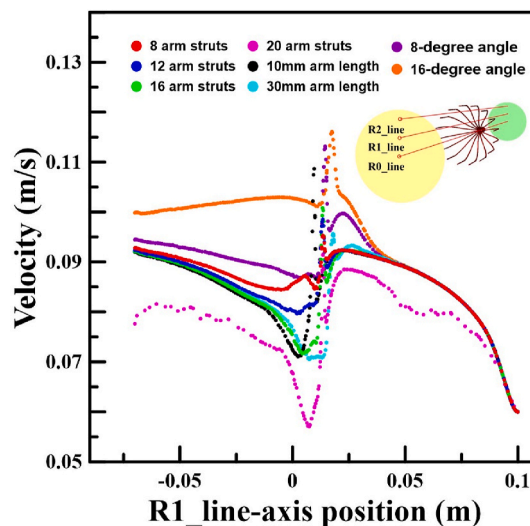

Fig. 12. Blood flow velocity on the eccentric line (R1_line) of the 8 cases.
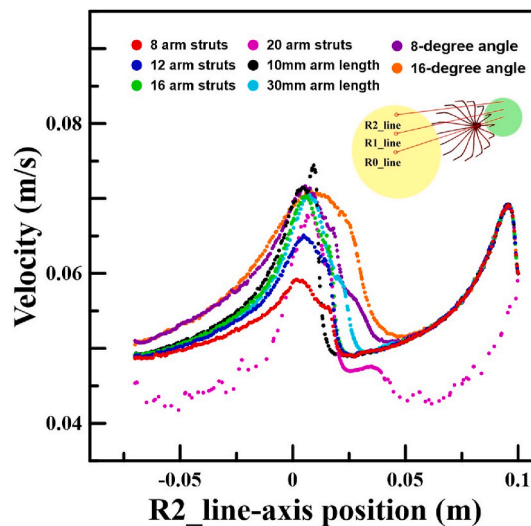
Fig. 13. Blood flow velocity on the eccentric line (R2_line) of the 8 cases.

changed to a speed smaller than 16 arm struts.

Second, in contrast to the above, for 10, 20, and 30 mm arm length, the speed decreases as the arm length increases. This is because the struts angle decreases, which brings the blood and the inner arm struts together earlier, in the order of 30, 20, and 10 mm arm length. The final speed is constant at about 0.048 m/s.

Third, as the tilted filter angle increases from 0 to 8–19°, the R2_line becomes more tilted and the imbalance in velocity flow across the filter wall worsens. This coincides with the blood meeting the internal struts earlier and at higher velocities overall. However, as shown in Fig. 10(c), the wall opposite the R2_line experiences a significantly larger low-velocity zone compared to other cases due to the tilted filter head.

3.2. Blood pressure

Clinically, the IVC wall is known to be very thin compared to the aorta, with low blood pressure and pulsation, making it relatively stable. (Leask et al., 2013). However, it is also easily influenced by various morphological parameters of the IVC. In this study, we confirmed the effects of IVCF on the vessel after surgery by CFD simulation.

Fig. 14 shows the total pressure distribution of an IVCF with 16 struts of four types inserted into the IVC. The overall blood flow forms a strong pressure streamline at the inlet, and the pressure is higher inside the struts and lower outside, which can be distinguished. The high pressure gathered inside the IVCF flows out through the arm struts, forming a low pressure at the head part and flowing out at a low pressure.

A comparison of the results of Fig. 14(a), (b), and (c) shows that (b), with shorter arm struts than (a), has the lowest static pressure in the head area, making it most likely to cause thrombosis. To explain further, short arm struts on IVC filters may be associated with a higher risk of thrombosis. Basic fluid dynamics, especially Bernoulli's principle, can be explained. Bernoulli's principle states that for an incompressible fluid like blood in steady flow, an increase in flow velocity corresponds to a decrease in static pressure. In simpler terms, when a fluid encounters a narrower passage, it has to speed up to maintain the same flow rate. This speeding up comes at the
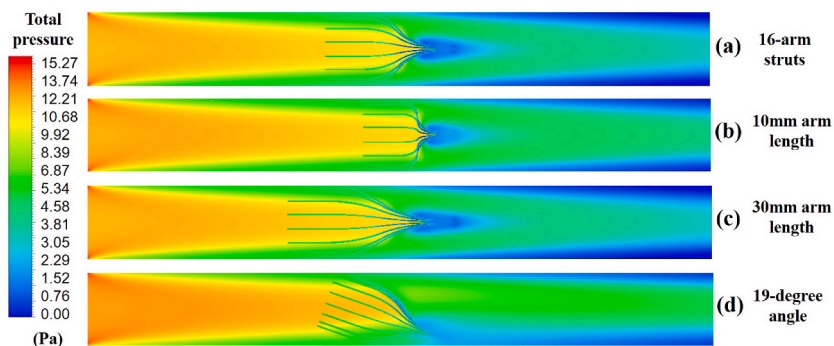

Fig. 14. Distribution of IVC total pressure with insertion of 4 types of IVCF.

cost of a decrease in pressure. That is, shorter arm braces create a smaller flow channel between the struts compared to longer braces. Blood flowing through this narrower channel experiences an increase in velocity according to Bernoulli's principle. Shorter arm braces create a smaller flow channel between the struts compared to longer braces. Therefore, reduced blood pressure around the filter may increase blood residence time and enhance clotting by promoting coagulation factor interaction, ultimately leading to thrombosis. (c), with the longest arm struts, creates the widest low static pressure area in the head area. And (d), with a head angle of 19°, has a very long low static pressure area along the wall where the head touches the wall, which can cause more complications, such as thrombosis formation on the wall. Therefore, among the four cases, (a), 16-arm struts IVCF, shows the best performance and safe values, with little stagnation and recirculation due to low pressure. Furthermore, the flow around the placed IVC filter is not affected by the existence of the filter, except for cases where the pressure near the filter is very close to the filter arm, struts, and head.

Figs. 15–17 illustrate the pressure distribution along the axial position of the IVC using both the central and eccentric lines. Among the three geometric parameters of the IVCF, an increasing number of struts leads to a high pressure of 10.5–13.5 Pa at the inlet of the central line (R0) in Fig. 15. This pressure then rapidly drops to 3.8 Pa at the point of first contact with the internal arm struts.

Blood flow after passing through the filter increases to about 6 Pa and then flows out of the outlet at a pressure of about 4.6 Pa. The increase in the number of struts at the centerline (R0) results in an increase in pressure until the blood flow first contacts the internal arm struts. In other areas, the pressure is similar. In addition, the increase in arm length resulted in similar pressure for 10 and 20 mm, with a slight difference of about 0.375 Pa at the point before it meets the internal arm struts for the first time at the inlet at 30 mm. Similarly to the previous results, the pressure distribution was similar for 0, 8, and 19° angles, with a slight difference at the inlet. Figs. 16 and 17 show the pressure distribution along the R1 and R2 lines, which are located between the centerline and the wall. The overall trend is similar to that of the R1 line. As the distance from the R0 line to the R2 line increases, i.e., as the distance from the center of the IVCF increases, the resistance to pressure becomes almost linear, as shown in Fig. 17. Therefore, the pressure drops sharply at the point where the blood flow meets the first strut inside the IVCF and in the central head region, making it the most likely location for the formation of a blood clot.

3.3. IVCF wall shear stress

The WSS of the IVCF was calculated based on velocity data through CFD calculations. Fig. 18 shows the wall shear stress resulting from the change of four shape parameters, such as 16, 20 arm struts, 10 mm arm length, and 19-degree angle. In all four geometries, WSS concentrates upstream of the filter arm due to flow acceleration around struts. The sudden jump in flow velocity gradient caused by the filter surface leads to a substantial rise in WSS inside the filter, as WSS is directly proportional to both velocity gradient and blood viscosity.

In particular, Fig. 18(b) the 20 arm struts showed the highest and widest WSS distribution, followed by Fig. 18(c) 10 mm arm length, Fig. 18(a) 16 arm struts, in terms of WSS distribution size. In Fig. 18(d) case of the filter with a tilted angle of 19°, it has high WSS in the filter tip part that first touches the blood and the diagonal arm struts that are tilted.

Fig. 19 shows the stress size distribution of WSS on the surface of the filter models in Fig. 18, depending on the location. The filters in Fig. 19(a), (b), and (d) are 0.35 m long, and the filter in Fig. 19(c) is 0.25 m long. The surface stress distribution of WSS for Fig. 19(a), (b), and (d), excluding the tilted filter (d), has a size of about 1 Pa from the Flow in part where blood enters to 0.025 m. This length is the internal struts that touch the Wall contact.

Then, as shown in the red part of Fig. 18(b), the arm struts have the highest surface WSS value at 0.015 m and then go down again to 0.005 m, where the head starts. As shown in Fig. 18(d), the tilted 19-degree angle has a surface WSS value of 4.5 Pa, which is similar to the value in the middle of the arm struts, from the filter tip part. It dropped to 0.025 m and then decreased, similar to the pattern of (a), (b), and (c), where it was highest in the middle of the arm struts and then decreased. Overall, the tilted filter (d) had a larger surface WSS area and the largest stress value than the other filters.

Higher WSS magnitude is associated with an increased risk of thrombosis and platelet activation, according to previous studies [31]. When high WSS exceeds the physiological range, it can damage or detach endothelial cells, disrupting the smooth endothelial surface and exposing the underlying basement membrane, which is more thrombogenic. This endothelial dysfunction can further be exacerbated by the release of inflammatory factors from the damaged cells, potentially leading to thrombosis. Additionally, high WSS can create localized areas of turbulence or recirculation zones near the filter struts. These zones can trap blood components, including platelets, and increase the risk of thrombus formation [41,42]. While higher WSS on the filter surface initially benefits thrombus clearance and PE prevention by dissolving larger clots, it carries the risk of triggering platelet activation and filter thrombosis due to high shear rates. Therefore, a high WSS value of IVCF is not always good, and it is better to be upright and in line with the IVC rather than tilted, which has a concentrated stress inside the filter.

Based on these studies, it is important to find a balance between a high enough WSS to help dissolve thrombi and a low enough WSS to prevent platelet activation. One way to do this is to use a filter with a design that minimizes the concentration of stress. For example, a filter that is upright and in line with the IVC will have a more uniform WSS distribution than a filter that is tilted. This can help to reduce the risk of platelet activation and filter thrombosis.

3.4. Molecular viscosity

Unlike common fluids, blood's viscosity changes with flow speed. The Carreau model accurately captures this behavior, working for both slow (thickening) and fast (thinning) blood flow. And rouleaux formation, promoted by low shear rates, increases the apparent size of red blood cells, leading to higher blood viscosity. This thickening effect is countered at high shear rates, where rouleaux break
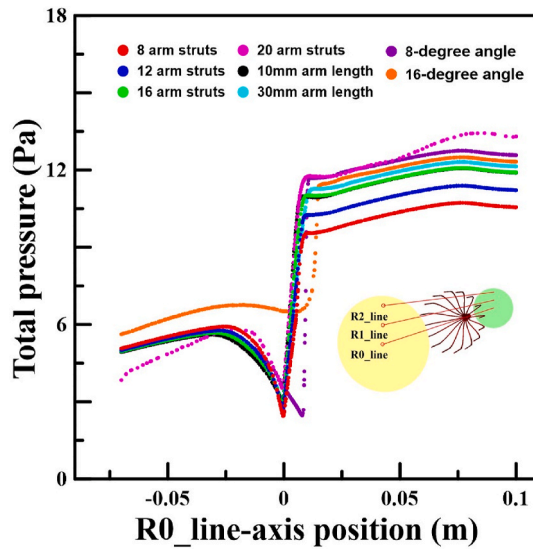
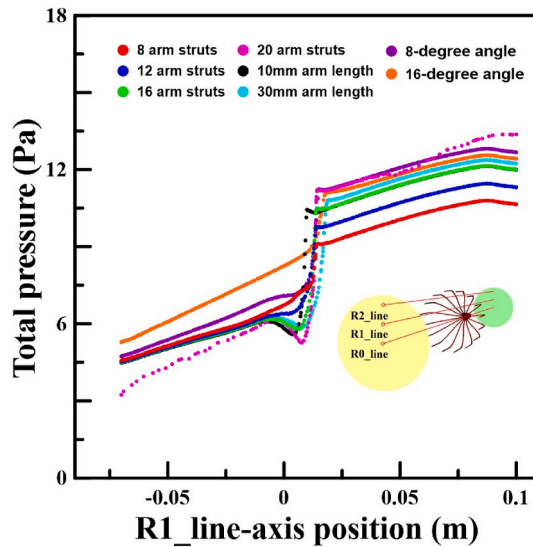**Fig. 15.** Total pressure on the central line (R0_line) of the 8 cases.

Fig. 16. Total pressure on the eccentric line (R1_line) of the 8 cases.

apart and cells deform, reducing their effective size and lowering blood viscosity [43].

Fig. 20 shows the step-by-step viscosity distribution of blood flowing through the 16-arm struts filter model ($\alpha = 0°$) with the best performance and the tilted 19-degree angle model. The viscosity distribution of the filter starts to develop from the center of the inner arm struts with high WSS, as shown in Fig. 20(a), and forms to the outer arm struts in Fig. 20(b). Therefore, the low shear rate in the gray area of step 1 leads to high viscosity outside the struts in steps 2 and 3, making it a prime candidate for thrombosis. Fig. 20(c) shows the case where the viscosity is particularly concentrated downstream of the filter head.

Fig. 20(d), (e), and (f) show the three-stage viscosity distribution of the tilted 19-degree angle filter. In Fig. 20(d), the viscosity of the blood flows first from the inner surface of the upper arm struts and the filter struts tips of the filter. As shown in Fig. 20(e) and (f), the viscosity gradually spreads diagonally from the inner upper arm struts and struts tips to the outer surface of the struts until it is fully extended. When blood cells in the filter form a blood clot, there is a high possibility that it will occur on the viscosity distribution external surface of the filter.

4. Limitations

The current CFD model used a simplified model that was not derived from a model of the IVC from CT or MRI, and did not consider
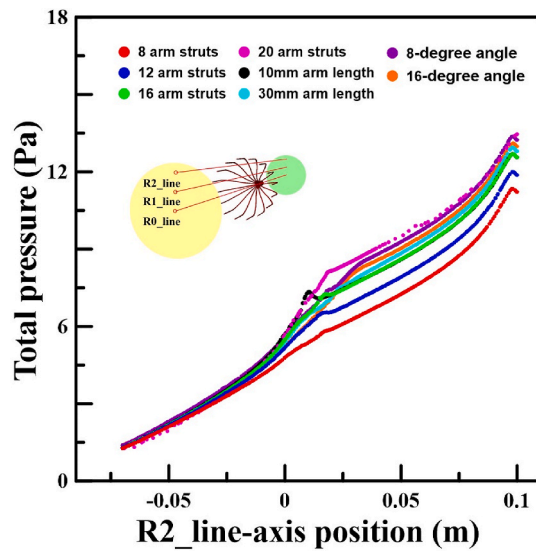
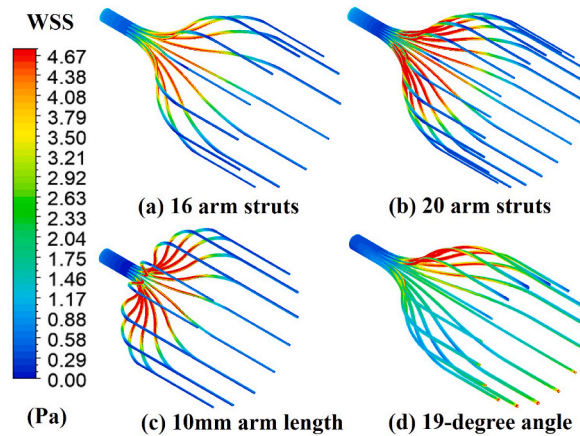**Fig. 17.** Total pressure on the eccentric line (R2_line) of the 8 cases.

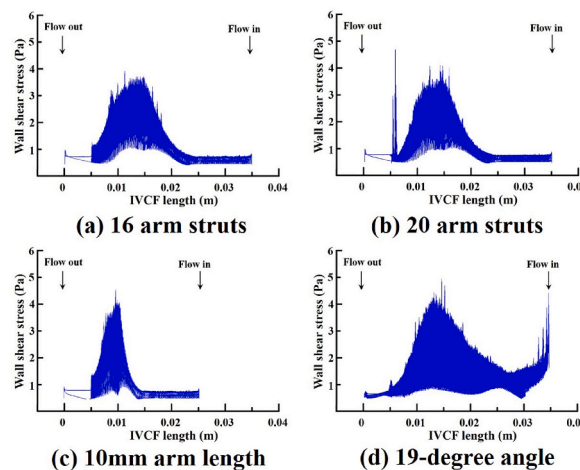**Fig. 18.** WSS distribution of IVCFs according to four shape parameters.

Fig. 19. The stress size distribution of WSS on the surface of the filter models, depending on the location.

16 arm struts

(a) Step 1   (b) Step 2   (c) Step 3

19-degree angle
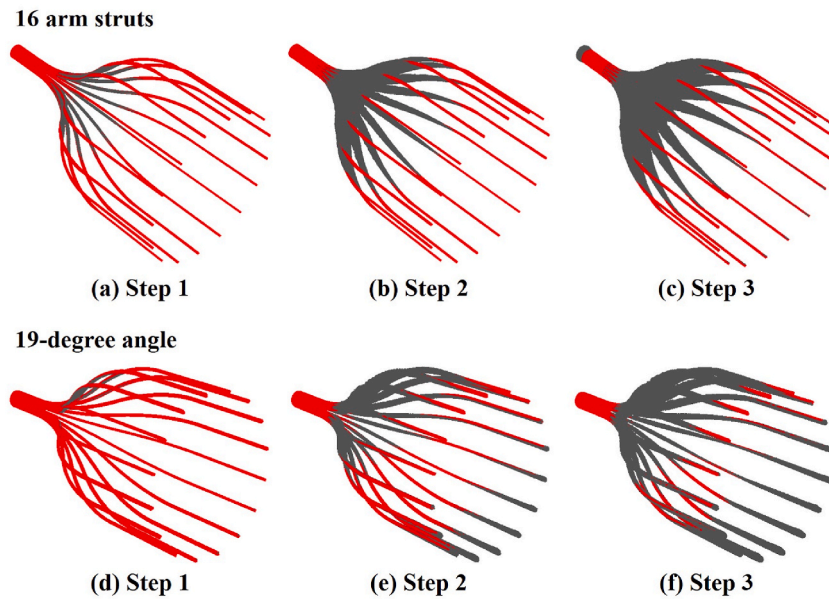
(d) Step 1   (e) Step 2   (f) Step 3

Fig. 20. The three-stage viscosity distribution of the 16-arm struts filter and the 19-degree angle filter model in blood flow.

factors such as pulsatile flow and vascular wall deformation. Future simulations should move closer to reality by incorporating distal side branches, IVC deformation, and the dynamic collapse caused by respiration, factors with a substantial influence on the results. This can be achieved by using real vessel data from diverse clinical patients. Despite the acceptability of average boundary conditions in this context, their inherent limitations in capturing the nuanced dynamics of blood flow necessitate the exploration of more sophisticated approaches in future investigations. And the parameters were used on a limited IVCF model, and the focus was on steady-state simulations, ignoring the pulsatile characteristics of blood flow. For more realistic simulations, it is necessary to apply pulsatile flow conditions. However, this study provides valuable insights into the design of IVCFs for improving hemodynamics and reducing the risk of thrombosis. By optimizing the number of struts, arm length, and tilt angle, filter placement can be customized for individual patients, potentially leading to safer and more effective treatment outcomes, and helping to reduce complications such as thrombosis.

5. Conclusion and discussion

The purpose of this study is to minimize the complications of DVT and PE by optimizing the hemodynamic analysis and design performance of IVCFs for VTE patients using CFD simulations. Therefore, the factors that have a significant impact on the location of thrombus formation within the filter, thrombus capture, dissolution, and hemodynamic flow, which have not yet been clearly studied, are as follows.

- Viscous Block Effect: When blood enters the IVCF, it experiences a viscous block effect due to the no-slip boundary condition and viscosity. This effect causes the velocity in the center of the filter to accelerate, and when it meets the struts, the velocity inside and outside the filter is quickly reversed. The blood flow between the struts is disrupted and dispersed, and flows out at a faster velocity, thus reducing the velocity inside the filter.
- Optimal Filter Design: The number of arm struts has a significant impact on the size of the stagnation and recirculation zones. As the number of struts increases, the volume of these zones increases, but the velocity of the blood at the point where it first encounters the arm does not increase proportionally. This is because the blood flow meets the struts at a sharp angle, which causes a sudden decrease in velocity. This can lead to stagnation and recirculation of blood near the filter head.

The length of the arm has the opposite effect. As the length of the arm increases, the size of the stagnation and recirculation zones decreases. This is because the blood has more time to accelerate before it reaches the struts. The shape of the head also changes from a blunt to a sharp streamline as the arm length increases.

Tilting the filter throws off the flow's equilibrium, creating stagnant and swirling blood regions near the head, which can have significant hemodynamic consequences. The flow of velocity and pressure is also greater towards the side of the filter that is tilted. In particular, the stagnation and low-velocity zones are more developed at the wall of the tilted filter. This can increase the residence time of blood particles, which can promote thrombus formation. All of these parameters interact with each other and influence each other.

Based on the results of this study, 16 arm struts with a length of 20 mm and a tilt angle of 0° provide the best balance between thrombus capture and minimization of hemodynamic disturbance. This configuration minimizes the size of the stagnation and recirculation zones while maintaining sufficient WSS for thrombus dissolution.

- WSS Distribution: As blood flow sped up around the filter arm struts, the rate of change in velocity (internal velocity gradient) intensified, leading to a significantly higher WSS on the upstream side compared to the downstream axis. This resulted in a markedly asymmetrical WSS distribution. A configuration of 16 arm struts with an arm length of 20 mm and a tilt angle of $0°$ presented the most balanced and wide WSS distribution. While high wall shear stress can activate platelets and lead to thrombosis, low WSS can promote thrombus accumulation. Additionally, tilted filters exhibit undesirable areas of concentrated stress, potentially causing blood clots on the vessel walls.
- Clinical Significance: The study findings suggest that careful consideration of filter design and placement is important to minimize hemodynamic complications and improve IVCF efficacy. Specifically, the study found that 16 arm struts with an arm length of 20 mm and a tilt angle of $0°$, with optimal strut number and length, can minimize complications such as DVT and PE when aligned vertically in the vessel [44,45]. The findings also suggest that CFD can be a useful tool for medical device, clinical, and in vitro research, making it more economical and faster than traditional methods.

This paper examines the design of the viscous block effect and its influence on IVCFs. We demonstrate how struts of varying number, length, and angle impact thrombus formation location, capture, dissolution, and hemodynamic flow within the filter. Importantly, these parameters also affect the shear stress on both the vessel wall and the filter itself. Optimizing these parameters was achieved through CFD simulations of non-Newtonian blood flow using the Carreau model. This enabled us to evaluate the performance of the filter and its surrounding flow, representing a novel approach not previously explored in experimental or computational studies. Our key findings include.

- CFD simulations were performed to evaluate the hemodynamic performance of the IVC filter using a hexahedral mesh for its excellent accuracy and speed. Mesh independence was assessed by comparing blood flow velocity and WSS in the blood vessel wall as mesh size increased using the Richardson extrapolation method. As the number of meshes increased, blood flow velocity increased gradually, with filters having 8, 12, 16, and 20 struts experiencing velocity increases ranging from 0.3 % to 1.5 %. Area-averaged WSS on the IVC wall decreased by 1.1 %–9.1 % as the number of meshes increased, while on the filter wall it increased by 0.1 %–4.8 %. Additionally, increasing the number of struts led to WSS increases on both the IVC wall and the filter wall.
- While increasing the number of struts increases the volume of stagnation and recirculation zones, the velocity of the downstream zone where blood first encounters the arm struts does not increase proportionally. This is due to the narrowed gaps between struts, causing blood flow to disperse and slow down. Conversely, as arm length increases, the volume of stagnation and recirculation zones decreases, while the velocity where blood first encounters the arm strut increases, reflecting the widening gaps and easier flow. Thus, all arm struts contribute to the viscous blocking effect, which accelerates blood flow inside the IVC and increases filter WSS. This effect can have significant hemodynamic consequences on thrombus entrapment, venous thrombosis, and flow impedance.
- When the IVCF is tilted, the symmetrical flow around the filter is disrupted, and the stagnation area around the filter head increases. This can be explained by the fact that the tilted filter directs blood flow towards one side of the vessel. Consequently, the flow velocity inside the filter increases on the opposite side as blood concentrates to one side, creating a pressure difference within the filter. At the maximum tilt angle of $α = 19°$, a large stagnant area forms around the filter head. This is because the completely tilted filter almost touches the vessel wall, making it difficult for blood flow to bypass the filter. Based on these findings, an angle of $α = 0°$, which maintains the IVCF in an upright position, is expected to be the most effective in preventing thrombus formation.
- Low shear rates promote the formation of rouleaux, structures of aggregated red blood cells that effectively increase fluid molecule size and viscosity. High shear rates, on the other hand, destroy these rouleaux and deform the RBCs into elongated shapes. Consequently, the high effective viscosity of the fluid has a higher probability of forming blood clots, especially on the side of the arm struts where the filter's viscosity distribution is high. Therefore, understanding the relationship between shear rate, rouleaux formation, and effective viscosity is crucial for designing effective blood filters and preventing thrombosis.

Data availability statement

No data was used for the research described in the article.

CRediT authorship contribution statement

Byeong-Jun Kim: Writing – original draft, Software, Methodology, Funding acquisition, Conceptualization. **Chiseung Lee:** Writing – review & editing, Validation, Supervision, Project administration.

Declaration of competing interest

The authors declare that they have no known competing financial interests or personal relationships that could have appeared to influence the work reported in this paper.

Acknowledgments

References

[1] M.A. Singer, S.L. Wang, D.P. Diachin, Design optimization of vena cava filters: an application to dual filtration devices, J. Biomech. Eng. 132 (10) (2010) 101006, https://doi.org/10.1115/1.4002488.
[2] Patel, et al., Pathogenesis and epidemiology of venous thromboembolic disease, Crit. Care Nurs. Q. 40 (3) (2017) 191–200, https://doi.org/10.1097/CNQ.0000000000000158.
[3] Grzegorz Kopeć, et al., Role of catheter-directed therapies in the treatment of acute pulmonary embolism. Expert opinion of the polish PERT initiative, working group on pulmonary circulation, association of cardiovascular interventions, and association of intensive cardiac care of the polish cardiac society, Pol. Heart J. 81 (4) (2023) 423–440, https://doi.org/10.33963/KP.a2023.0075.
[4] H.M. Alshaqaq, A.M. Al-Sharydah, M.S. Alshahrani, S.M. Alqahtani, M. Amer, Prophylactic inferior vena cava filters for venous thromboembolism in adults with trauma: an updated systematic review and meta-analysis, J. Intensive Care Med. 38 (6) (2023) 491–510, https://doi.org/10.1177/08850666231163141.
[5] Vijay V. Kakkar, Philip C. Adams, Preventive and therapeutic approach to venous thromboembolic disease and pulmonary embolism can death from pulmonary embolism be prevented? J. Am. Coll. Cardiol. 8 (6) (1986) 146B–158B, https://doi.org/10.1016/S0735-1097(86)80016-X.
[6] Fisal Asiri, Md Irfanul Haque Siddiqui, Masood Ashraf Ali, Tabish Alam, Dan Dobrotă, Radu Chicea, Robert Daniel Dobrotă, Mathematical modeling of active contraction of the human cardiac myocyte: a review, Heliyon 9 (9) (2023) e20065, https://doi.org/10.1016/j.heliyon.2023.e20065.
[7] Md Irfanul Haque Siddiqui, Abdullah Alnaser Ibrahim, Alluhydan Khalid, Assessment of a carbon fiber prosthetic running blade for enhanced reliability, Eksploatacja i Niezawodność-Maintenance and Reliability 25 (4) (2023) 172668, https://doi.org/10.17531/ein/172668.
[8] S.F.C. Stewart, R.A. Robinson, R.A. Nelson, et al., Effects of thrombosed vena cava filters on blood flow: flow visualization and numerical modeling, Ann. Biomed. Eng. 36 (2008) 1764–1781, https://doi.org/10.1007/s10439-008-9560-6.
[9] J. Bajda, A.N. Park, A. Raj, R. Raj, V.R. Gorantla, Inferior vena cava filters and complications: a systematic review, Cureus 15 (6) (2023) e40038, https://doi.org/10.7759/cureus.40038, 6.
[10] K.I. Aycock, R.L. Campbell, K.B. Manning, S.P. Sastry, S.M. Shontz, F.C. Lynch, B.A. Craven, A computational method for predicting inferior vena cava filter performance on a patient-specific basis, ASME. J Biomech Eng 36 (8) (2014) 081003, https://doi.org/10.1115/1.4027612.
[11] Jessica M. Andreoli, Bartley G. Thornburg, Ryan M. Hickey, Inferior vena cava filter–related thrombus/deep vein thrombosis: data and management, Semin. Intervent. Radiol. 33 (2) (2016) 101–104, 0.1055/s-0036-1581087.
[12] Richard L. Leask, K. Wayne Johnston, Matadial Ojha, Hemodynamic effects of clot entrapment in the trap, Ease Inferior Vena Cava Filter 15 (5) (2004) 485–490, https://doi.org/10.1097/01.RVI.0000124941.58200.85.
[13] Shiyue Zhang, Xue Song, Jingying Wang, Wen Huang, Yue Zhou, Mingrui Li, CFD Study on Hemodynamic Characteristics of Inferior Vena Cava Filter Affected by Blood Vessel Diameter, vol. 20, 2023, pp. 81–94, https://doi.org/10.32604/mcb.2023.044445, 2.
[14] Jafar Moradicheghamahi, Muhammad Qasim, Sohrab Jafarpour, Hamed Farokhi, Investigation of the effects of an inferior vena cava filter and captured clot size on the hemodynamic parameters in non-Newtonian turbulent pulsatile blood flow, Applied Bionics and Biomechanics. 2349775 (2023) 18, https://doi.org/10.1155/2023/2439775.
[15] Erica L. Schwarz, Luca Pegolotti, Martin R. Pfaller, Alison L. Marsden, Beyond CFD: emerging methodologies for predictive simulation in cardiovascular health and disease, Biophysics Rev 4 (1) (2023) 011301, https://doi.org/10.1063/5.0109400.
[16] B.A. Herbig, S.L. Diamond, Thrombi produced in stagnation point flows have a core-shell structure, Cell. Mol. Bioeng. 10 (6) (2017) 515–521, https://doi.org/10.1007/s12195-017-0503-x.
[17] Lauren D.C. Casa, David H. Deaton, David N. Ku, Role of high shear rate in thrombosis, J. Vasc. Surg. 61 (4) (2015) 1068–1080, https://doi.org/10.1016/j.jvs.2014.12.050.
[18] J. He, Z. Wang, Y.X. Zhou, H. Ni, X. Sun, J. Xue, S. Chen, S. Wang, M. Niu, The application of inferior vena cava filters in orthopaedics and current research advances, Front. Bioeng. Biotechnol. 10 (2022) 1045220, https://doi.org/10.3389/fbioe.2022.1045220.
[19] L. Duffett, M. Carrier, Inferior vena cava filters, J. Thromb. Haemostasis 15 (1) (2017) 3–12, https://doi.org/10.1111/jth.13564.
[20] Brent Craven, Jason Weaver, Tom Duerig, Bonsignore Craig, Karthikeyan Senthilnathan Kenneth Aycock, Generic-IVC-filter. US FDA Confluent Medical, 2017. https://github.com/kenaycock/Generic-IVC-Filter.
[21] E. Tedaldi, C. Montanari, K.I. Aycock, F. Sturla, A. Redaelli, K.B. Manning, An experimental and computational study of the inferior vena cava hemodynamics under respiratory-induced collapse of the infrarenal IVC, Med. Eng. Phys. 54 (2018) 44–55, https://doi.org/10.1016/j.medengphy.2018.02.003.
[22] L. Muller, X. Bobbia, M. Toumi, et al., Respiratory variations of inferior vena cava diameter to predict fluid responsiveness in spontaneously breathing patients with acute circulatory failure: need for a cautious use, Crit. Care 16 (2012) 188, https://doi.org/10.1186/cc11672.
[23] D. Gallo, G. De Santis, F. Negri, et al., On the use of in vivo measured flow rates as boundary conditions for image-based hemodynamic models of the human aorta: implications for indicators of abnormal flow, Ann. Biomed. Eng. 40 (2012) 729–741, https://doi.org/10.1007/s10439-011-0431-1.
[24] N. Kumar, A. Khader, R. Pai, et al., Computational fluid dynamic study on effect of Carreau-Yasuda and Newtonian blood viscosity models on hemodynamic parameters, J. Comput. Methods Sci. Eng. 19 (2) (2019) 465–477, https://doi.org/10.3233/jcm-181004.
[25] Z. Ren, S.L. Wang, M.A. Singer, Modeling hemodynamics in an unoccluded and partially occluded inferior vena cava under rest and exercise conditions, Med. Biol. Eng. Comput. 50 (2012) 277–287, https://doi.org/10.1007/s11517-012-0867-y.
[26] A. Fuchs, N. Berg, L. Fuchs, L. Prahl Wittberg, Assessment of rheological models applied to blood flow in human thoracic aorta, Bioengineering 10 (11) (2023) 1240, https://doi.org/10.3390/bioengineering10111240.
[27] M.G. Al-Azawy, S.K. Kadhim, A.S. Hameed, Newtonian and non-Newtonian blood rheology inside a model of stenosis, CFD Lett. 12 (11) (2020) 27–36, https://doi.org/10.37934/cfdl.12.11.2736.
[28] K.I. Aycock, R.L. Campbell, F.C. Lynch, K.B. Manning, B.A. Craven, The importance of hemorheology and patient anatomy on the hemodynamics in the inferior vena cava, Ann. Biomed. Eng. 44 (2016) 3568–3582, https://doi.org/10.1007/s10439-016-1663-x.
[29] S. Tabakova, E. Nikolova, S. Radev, Carreau model for oscillatory blood flow in a tube, AIP Conf. Proc. 1629 (2014) 336–343, https://doi.org/10.1063/1.4902290.
[30] C. Alberto Figueroa, Irene E. Vignon-Clementel, Kenneth E. Jansen, Thomas J.R. Hughes, Charles A. Taylor, A coupled momentum method for modeling blood flow in three-dimensional deformable arteries, Comput. Methods Appl. Mech. Eng. 195 (41–43) (2006) 5685–5706, https://doi.org/10.1016/j.cma.2005.11.011.
[31] K. Wang, C.H. Armour, R.G.J. Gibbs, et al., A numerical study of the effect of thrombus breakdown on predicted thrombus formation and growth, Biomech. Model. Mechanobiol. (2023), https://doi.org/10.1007/s10237-023-01757-8.
[32] Michael A. Singer, Stephen L. Wang, Modeling blood flow in a tilted inferior vena cava filter: does tilt adversely affect hemodynamics? J. Vasc. Intervent. Radiol. 22 (2) (2011) 229–235, https://doi.org/10.1016/j.jvir.2010.09.032.
[33] Jian Wen, Kiao Inthavong, Jiyuan Tu, Simin Wang, Numerical simulations for detailed airflow dynamics in a human nasal cavity, Respir. Physiol. Neurobiol. 161 (2) (2008) 125–135, https://doi.org/10.1016/j.resp.2008.01.012.
[34] Marko Krstic, Lana Pantic, Stefan Djordjevic, Ivana Radonjic, Veljko Begovic, Branka Radovanovic, Marko Mancic, Passive cooling of photovoltaic panel by aluminum heat sinks and numerical simulation, Ain Shams Eng. J. 15 (1) (2024) 102330, https://doi.org/10.1016/j.asej.2023.102330.
[35] M. Ahmadi, A. Ghaderi, H. MohammadNezhad, A. Kuriqi, S. Di Francesco, Numerical investigation of hydraulics in a vertical slot fishway with upgraded configurations, Water 13 (19) (2021) 2711, https://doi.org/10.3390/w13192711.

[36] M. Spiegel, T. Redel, Y.J. Zhang, T. Struffert, J. Hornegger, R.G. Grossman, C. Karmonik, Tetrahedral vs. polyhedral mesh size evaluation on flow velocity and wall shear stress for cerebral hemodynamic simulation, Comput. Methods Biomech. Biomed. Eng. 14 (1) (2011) 9–22, https://doi.org/10.1080/10255842.2010.518565.

[37] Hegui Zhang, Siyang Tang, Hairong Yue, et al., Comparison of computational fluid dynamic simulation of a stirred tank with polyhedral and tetrahedral meshes, Iran. J. Chem. Chem. Eng. (Int. Engl. Ed.) 39 (4) (2020) 311–319, https://doi.org/10.30492/ijcce.2019.34950.

[38] Shan Wang, J. González-Cao, H. Islam, M. Gómez-Gesteira, C. Guedes Soares, Uncertainty estimation of mesh-free and mesh-based simulations of the dynamics of floaters, Ocean Eng. 256 (2022) 111386, https://doi.org/10.1016/j.oceaneng.2022.111386.

[39] J. Wang, W. Huang, Y. Zhou, F. Han, D. Ke, C. Lee, Hemodynamic analysis of VenaTech convertible vena cava filters using computational fluid dynamics, Biotechnology and Frontiers in Biotechnology 8 (2020) 556110, https://doi.org/10.3389/fbioe.2020.556110.

[40] M. Li, J. Wang, W. Huang, Y. Zhou, X. Song, Evaluation of hemodynamic effects of different inferior vena cava filter heads using computational fluid dynamics, Frontiers in Biotechnology and Biotechnology 10 (2022) 1034120, https://doi.org/10.3389/fbioe.2022.1034120.

[41] M. Zhou, Y. Yu, R. Chen, X. Liu, Y. Hu, Z. Ma, L. Gao, W. Jian, L. Wang, Wall shear stress and its role in atherosclerosis, Front Cardiovasc Med 3 (10) (2023) 1083547, https://doi.org/10.3389/fcvm.2023.1083547.

[42] K. Urschel, M. Tauchi, S. Achenbach, B. Dietel, Investigation of wall shear stress in cardiovascular research and in clinical practice-from bench to bedside, Int. J. Mol. Sci. 22 (11) (2021) 5635, https://doi.org/10.3390/ijms22115635.

[43] K.I. Aycock, *Towards Patient-Specific Modeling of Inferior Vena Cava Filter Performance*. Available from ProQuest Dissertations & Theses Global; ProQuest One Academic, 2016 2203505407. Retrieved from, https://www.proquest.com/dissertations-theses/towards-patient-specific-modeling-inferior-vena/docview/2203505407/se-2.

[44] Lara N. Roberts, Roopen Arya, Deep vein thrombosis and pulmonary embolism: diagnosis, treatment and prevention, Clin. Med. 11 (5) (2011) 465–466, https://doi.org/10.7861/clinmedicine.11-5-465.

[45] R. Bauersachs, Lungenembolie Beinvenenthrombose, Deep vein thrombosis and pulmonary embolism:Diagnosis and treatment, Inn. Med. 63 (6) (2022) 601–611, https://doi.org/10.1007/s00108-022-01349-1.